

Multi-Frame Image Restoration

Timothy J. Schulz
Michigan Technological
University

| | | |
|---|---|-----|
| 1 | Introduction..... | 219 |
| 2 | Mathematic Models | 221 |
| | 2.1 Image Blur and Sampling • 2.2 Noise Models | |
| 3 | The Multi-Frame Restoration Problem | 224 |
| | 3.1 Restoration as an Optimization Problem • 3.2 Linear Methods • 3.3 Nonlinear (Iterative) Methods | |
| 4 | Nuisance Parameters and Blind Restoration..... | 228 |
| 5 | Applications | 229 |
| | 5.1 Fine-Resolution Imaging from Undersampled Image Sequences • 5.2 Ground-based Imaging through Atmospheric Turbulence • 5.3 Ground-based Solar Imaging with Phase Diversity | |
| | Acknowledgments | 233 |
| | References | 233 |

1 Introduction

Multi-frame image restoration is concerned with the improvement of imagery acquired in the presence of varying degradations. The degradations can arise from a variety of factors — common examples include undersampling of the image data, uncontrolled platform or scene motion, system aberrations and instabilities, and wave propagation through atmospheric turbulence. In a typical application, a sequence of images (frames) is recorded about a static object or scene, and a single restored image is extracted through analog or digital signal processing. This is different from video processing as addressed in Chapters 3.9 and 3.10, which often deals with the restoration of a time-varying object or scene; and different from multichannel processing as addressed in Chapter 3.6, which often deals with the restoration of an object or scene that is viewed in fundamentally different ways, such as multiple view angles, wavelengths, polarizations, or resolutions. Simply stated, the goal of multi-frame image restoration is to process a sequence of blurred imagery of a static object or scene with the purpose of recovering a single deblurred image.

In most situations digital data are acquired, and the restoration processing is carried out by a general- or special-purpose digital computer. The general idea is depicted in Fig. 1, and

the following examples illustrate applications for which multi-frame restoration is utilized.

Example 1.1 (Resolution Improvement in Undersampled Systems) A critical factor in the design of visible and infrared imaging systems is often the trade-off between field-of-view and pixel size. The pixel size for a fixed detector array becomes larger as the field-of-view is increased, and the need for a large field-of-view can result in under-sampled imagery. This phenomena is illustrated in Fig. 2. One way to overcome the effects of larger pixels while preserving field of view is to utilize controlled or uncontrolled pointing jitter. In the presence of sub-pixel translations, a sequence of image frames can be processed to estimate the image values on a grid much smaller than the physical size of the detector pixels. Uncontrolled motion, however, presents the additional challenge of motion identification or the determination of optical flow. Often referred to as microscanning, the idea of processing a sequence of under-sampled image frames to restore resolution has received attention in a variety of applications [1, 2].

Example 1.2 (Imaging Through Turbulence) Spatial and temporal variations in the temperature of Earth's atmosphere cause the refractive index at optical wavelengths to vary in a random and unpredictable manner. Because of this, imagery

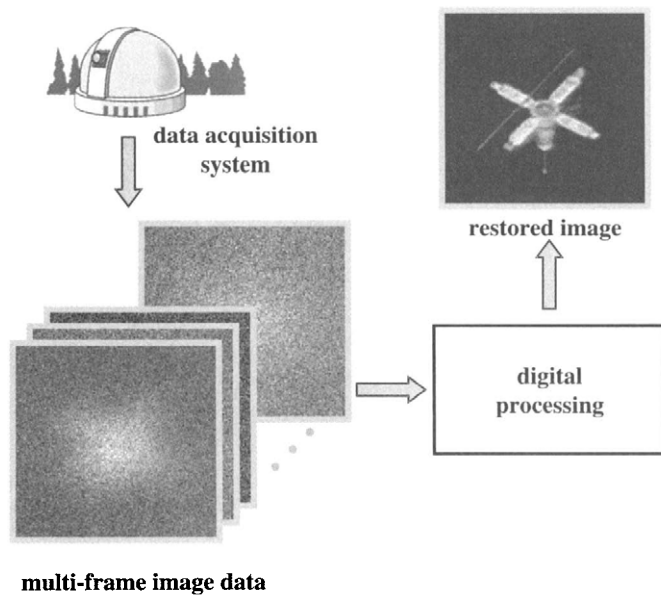


FIGURE 1 A general scenario in which multi-frame data are recorded and a restored image is produced through digital image processing.

acquired with ground-based telescopes can exhibit severe, time-varying distortions. A sequence of short exposure image frames will exhibit blurs such as those shown in Fig. 3, and the goal of a multi-frame image restoration procedure is to form a fine-resolution estimate of the object's reflectance from the noisy, blurred frames. Because the point-spread functions are not easily measured or predicted, this problem is often referred to as one of multi-frame blind deconvolution [3].

Many methods have been proposed and studied for solving multi-frame restoration problems — see, for example, references [4, 5] and those cited within. Well established restoration methods exist for situations in which all sources of blur and degradation are known or easily predicted. Some of the more popular techniques include regularized least squares and Wiener methods [4], and multi-frame extensions of the iterative Richardson–Lucy method [6]. When some of the system parameters are unknown, however, the problem becomes much more difficult. In this situation, the recovery of the object intensity can be called a multi-frame *blind* restoration problem because, in addition to the object

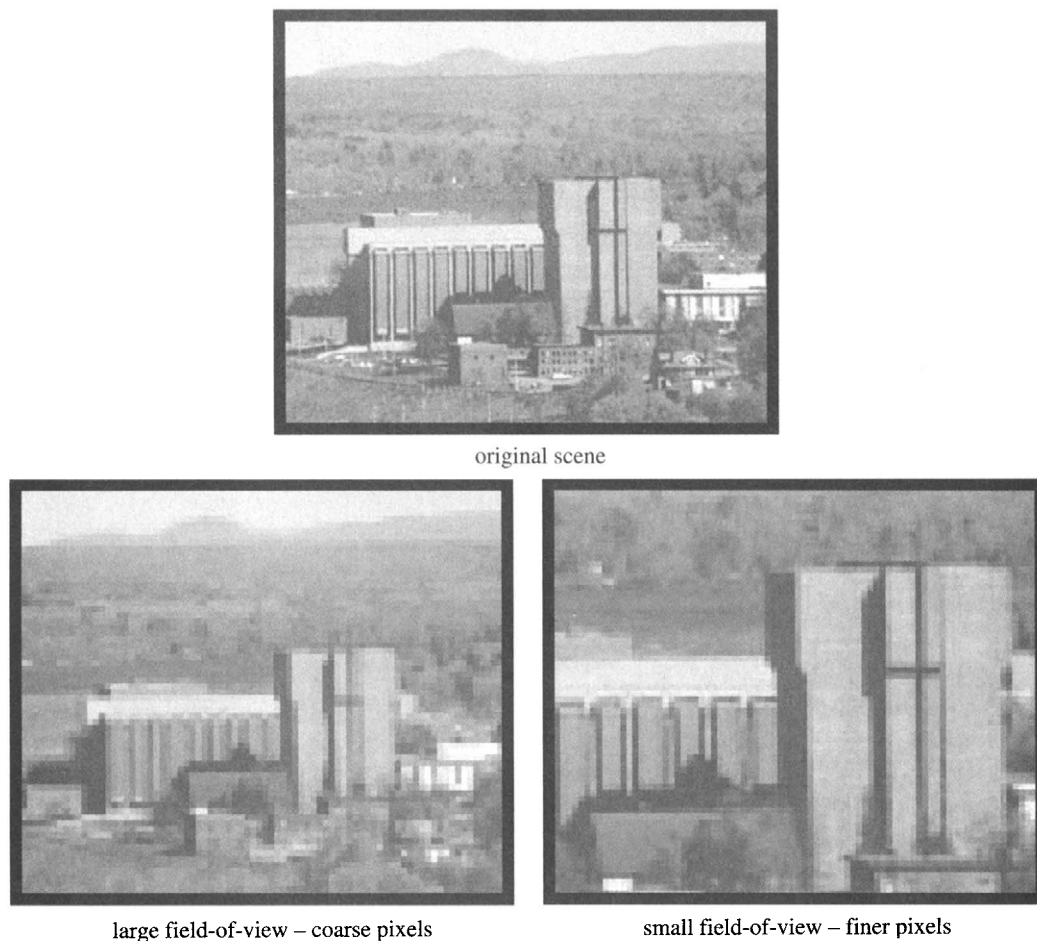


FIGURE 2 An illustration of the trade-off between field-of-view and pixel size. For a fixed number of pixels, the larger field-of-view results in coarse sampling — finer sampling leads to a smaller field-of-view.

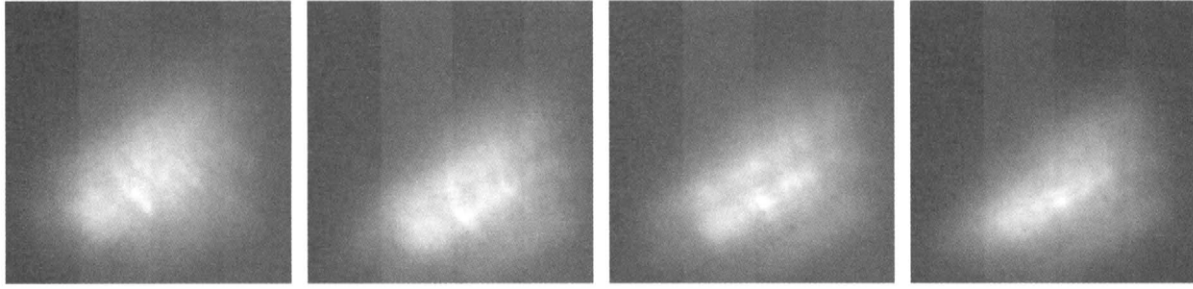


FIGURE 3 Imagery of the Hubble Space Telescope as acquired by a 1.6 m telescope at the Air Force Maui Optical Station.

intensity, the unknown system parameters must also be estimated [1–3, 7].

In the remainder of this chapter, we will develop mathematic models for the multi-frame imaging process, pose the multi-frame restoration problem as one of numeric optimization, provide an overview of restoration methods for non-blind and blind situations, and illustrate the methods with some current examples of multi-frame blind restoration.

2 Mathematic Models

The imaging problems discussed in this chapter all involve the detection and processing of electromagnetic fields after reflection or emission from a remote object or scene. Furthermore, the applications considered here are all examples of planar *incoherent imaging*, wherein the object or scene is characterized by its incoherent reflectance or emission function $f(\mathbf{x})$, $\mathbf{x} \in \mathcal{R}^2$. Throughout this chapter we will refer to f as the *image intensity* — a nonnegative function that represents an object's ability to reflect or emit light (or other electromagnetic radiation). The central task of a multi-frame image restoration problem, then, is the estimation of this intensity function from a sequence of noisy, blurred images.

2.1 Image Blur and Sampling

As illustrated in Fig. 4, the need for image restoration is, in general, motivated by two factors: i) system and environmental

blur; and ii) detector sampling. In the absence of noise, these two stages of image formation are described as follows.

- **System and Environmental Blur:**

In all imaging applications, the signal available for detection is not the image intensity f . Instead, f is blurred by the imaging system, and the observable signal is:

$$g_c(\mathbf{y}; \theta_t) = \int h(\mathbf{y}, \mathbf{x}; \theta_t) f(\mathbf{x}) d\mathbf{x}, \quad (1)$$

where $h(\mathbf{y}, \mathbf{x}; \theta_t)$ denotes the (generally time-varying) system and environmental point-spread function, $g_c(\mathbf{y}; \theta_t)$ denotes the (generally time-varying) continuous-domain intensity that results due to the blur, \mathbf{x} and \mathbf{y} are continuous-domain spatial coordinates, and θ_t denotes a set of time-varying parameters that determine the form of the point-spread function. The role of these parameters is discussed in more detail later in this chapter. Many applications involve *space-invariant* blurs for which the point-spread function depends only on the spatial difference $\mathbf{y} - \mathbf{x}$, and not on the absolute positions \mathbf{y} and \mathbf{x} . When this occurs the point-spread is written as a function of only one spatial variable, and the continuous-domain intensity is formed through a convolution relationship with the image intensity:

$$g_c(\mathbf{y}; \theta_t) = \int h(\mathbf{y} - \mathbf{x}; \theta_t) f(\mathbf{x}) d\mathbf{x}. \quad (2)$$

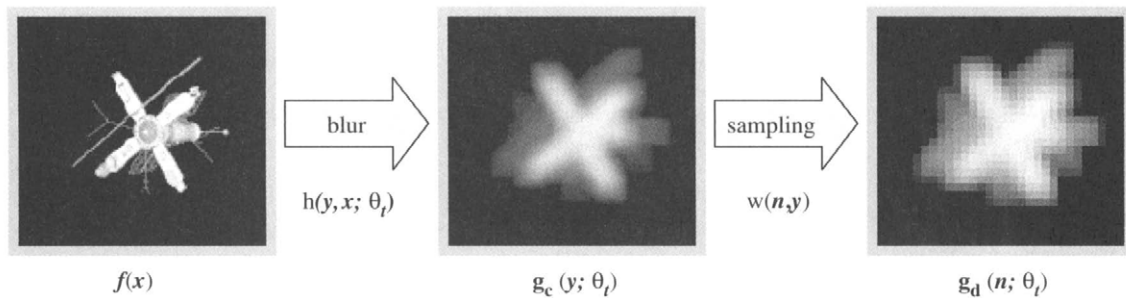


FIGURE 4 Pictorial representation of the image degradations due to system/environmental blur and detector sampling.

Diffraction is the most common form of image blur and its effects are present in every application involving remotely sensed image data. For narrowband, incoherent imaging-systems such as telescopes, microscopes, and infrared or visible cameras, the point-spread function for diffraction is modeled by the space-invariant function:

$$h(\mathbf{y}) = \left| \int A(\mathbf{u}) e^{-j\frac{2\pi}{\lambda f} \mathbf{u} \cdot \mathbf{y}} d\mathbf{u} \right|^2, \quad (3)$$

where $A(\mathbf{u})$ is the system's aperture function, \mathbf{u} is a two-dimensional spatial variable in the aperture plane, λ is the nominal wavelength of the detected radiation, and f is the system focal length. The notation $\mathbf{u} \cdot \mathbf{y}$ denotes the inner product operation, and is defined for two-dimensional spatial variables as:

$$\mathbf{u} \cdot \mathbf{y} = u_1 y_1 + u_2 y_2. \quad (4)$$

The use of this model for diffraction implicitly requires that the image intensity be spatially magnified by the factor $-f/r$, where r is the distance from the object or scene to the sensor. For a circular aperture of diameter D , the diffraction-limited point-spread function is the isotropic Airy pattern whose one-dimensional cross section is shown in Fig. 5. Due to the location of the first zero relative to the central peak, the resolution of a diffraction-limited system with a circular aperture is often cited as $1.22r\lambda/D$. This definition of resolution is, however, very arbitrary. Nevertheless, decreasing the wavelength, increasing the aperture diameter, or decreasing the distance to the scene will result in a narrowing of the point-spread function and an improvement in imaging resolution.

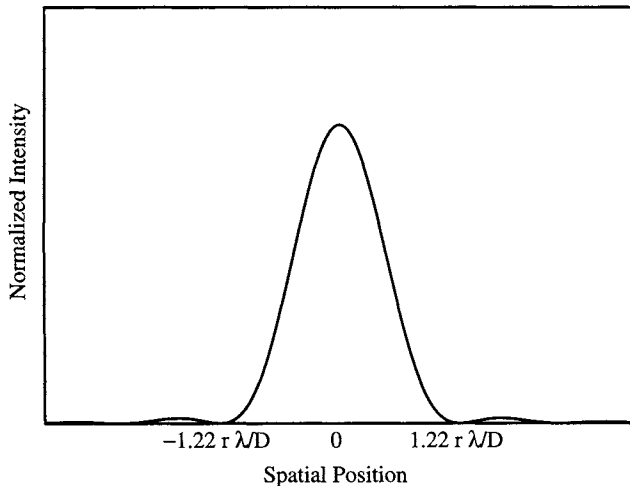


FIGURE 5 Cross section of the Airy diffraction pattern for a circular aperture.

Imaging systems often suffer from various types of optical aberrations — imperfections in the figure of the system's focusing element (usually a mirror or lens). When this happens, the point spread function takes the form:

$$h(\mathbf{y}; \theta) = \left| \int A(\mathbf{u}) e^{j\theta(\mathbf{u})} e^{-j\frac{2\pi}{\lambda f} \mathbf{u} \cdot \mathbf{y}} d\mathbf{u} \right|^2, \quad (5)$$

where $\theta(\mathbf{u})$ is the aberration function, often measured in units of *waves*.¹ Here, the notation $h(\mathbf{y}; \theta)$ explicitly shows the dependence of the aberrated point-spread function on the aberration function θ . An out-of-focus blur induces a quadratic aberration function:

$$\theta(\mathbf{u}) = \frac{\pi}{\lambda} \left(\frac{1}{r} + \frac{1}{d} - \frac{1}{f} \right) |\mathbf{u}|^2, \quad (6)$$

where r is the distance to the scene, d is the focal setting, and f is the focal length. This blur is reduced to diffraction when the “imaging equation” is satisfied and the system is in focus: $\frac{1}{r} + \frac{1}{d} = \frac{1}{f}$. Spherical aberration, such as that present in the Hubble Space Telescope's infamous primary mirror, induces a fourth-order aberration function:

$$\theta(\mathbf{u}) = B|\mathbf{u}|^4, \quad (7)$$

where the constant B determines the strength of the aberration. By setting the aberration to

$$\theta(\mathbf{u}) = \frac{2\pi}{\lambda f} \Delta \cdot \mathbf{u}, \quad (8)$$

this model can also be used to represent a tilt or pointing error Δ , so that

$$h(\mathbf{y}; \theta) = h(\mathbf{y} - \Delta). \quad (9)$$

Wave propagation through an inhomogeneous medium such as Earth's atmosphere can induce additional distortions. These distortions are due to temperature-induced variations in the atmosphere's refractive index, and are frequently modeled in a manner similar to that used for system aberrations:

$$h(\mathbf{y}; \theta_t) = \left| \int A(\mathbf{u}) e^{j\theta_t(\mathbf{u})} e^{-j\frac{2\pi}{\lambda f} \mathbf{u} \cdot \mathbf{y}} d\mathbf{u} \right|^2, \quad (10)$$

where the aberration function $\theta_t(\mathbf{u})$ can now vary with time. A typical diffraction-limited point-spread function along with a sequence of turbulence degraded point-spread functions are shown in Fig. 6.

¹One wave of aberration corresponds to $\theta(\mathbf{u}) = 2\pi$.

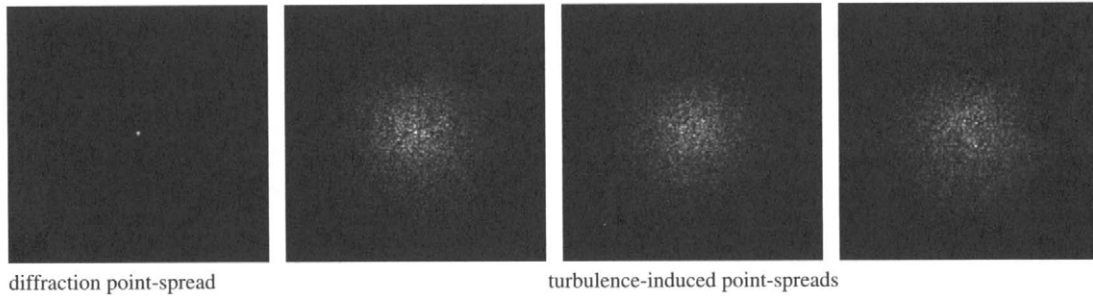


FIGURE 6 Diffraction-limited point-spread function and a typical sequence of turbulence-induced point-spread functions.

Another interesting perturbation to the diffraction-limited point-spread function can arise because of time-varying translations and rotations between the sensor and scene. In this case, the continuous-domain intensity is modeled as

$$g_c(\mathbf{y}; \theta_t) = \int h(\mathbf{y} - \mathbf{x}) f[\mathbf{A}(\phi_t)\mathbf{x} - \Delta_t] d\mathbf{x}, \quad (11)$$

where Δ_t represents a two-dimensional, time-varying translation, and

$$\mathbf{A}(\phi_t) = \begin{bmatrix} \cos(\phi_t) & -\sin(\phi_t) \\ \sin(\phi_t) & \cos(\phi_t) \end{bmatrix}, \quad (12)$$

is a time-varying rotation matrix (at angle ϕ_t). A simple change of variables leads to

$$g_c(\mathbf{y}; \theta_t) = \int h[\mathbf{y} - \mathbf{A}^{-1}(\phi_t)(\mathbf{x} + \Delta_t)] f(\mathbf{x}) d\mathbf{x}, \quad (13)$$

so that the shift variant point-spread function can be written as

$$h(\mathbf{y}, \mathbf{x}; \theta_t) = h[\mathbf{y} - \mathbf{A}^{-1}(\phi_t)(\mathbf{x} + \Delta_t)], \quad (14)$$

and the parameters characterizing the point-spread function are then $\theta_t = (\Delta_t, \phi_t)$.

Without loss of generality, we will model the system and environmental point-spread function as the (possibly) space-variant function $h(\mathbf{y}, \mathbf{x}; \theta_t)$, and note that this model captures diffraction, system aberrations, time-varying translations and rotations, and environmental distortions such as atmospheric turbulence. The parameter θ_t may be a simple vector parameter, or a more complicated parameterization of a two-dimensional function. Many times θ_t will not be well known or predicted, and the identification of this parameter can be one of the most challenging aspects of a multi-frame image restoration problem.

- **Sampling:**

The detection of imagery with discrete detector arrays results in the measurement of the (time-varying)

sampled intensity:

$$g_d(\mathbf{n}; \theta_t) = \int w(\mathbf{n}, \mathbf{y}) g_c(\mathbf{y}; \theta_t) d\mathbf{y}, \quad (15)$$

where $w(\mathbf{n}, \mathbf{y})$ is the response function for the \mathbf{n} th pixel in the image detector array, \mathbf{n} is a discrete-domain spatial coordinate, and $g_d(\mathbf{n}; \theta_t)$ is the discrete-domain intensity that results due to sampling of the continuous-domain, blurred intensity. The response function for an incoherent detector element is often of the form:

$$w(\mathbf{n}, \mathbf{y}) = \begin{cases} 1 & \mathbf{y} \in \mathcal{Y}_n \\ 0 & \mathbf{y} \notin \mathcal{Y}_n \end{cases}, \quad (16)$$

where \mathcal{Y}_n denotes the spatial region of integration for the \mathbf{n} th detector element. The regions of integration for most detectors are typically square or rectangular regions centered about the detector locations $\{\mathbf{y}_n\}$.

The combined effects of blur and sampling are modeled as:

$$\begin{aligned} g_d(\mathbf{n}; \theta_t) &= \int w(\mathbf{n}, \mathbf{y}) \int h(\mathbf{y}, \mathbf{x}; \theta_t) f(\mathbf{x}) d\mathbf{x} d\mathbf{y} \\ &= \int \left[\int w(\mathbf{n}, \mathbf{y}) h(\mathbf{y}, \mathbf{x}; \theta_t) d\mathbf{y} \right] f(\mathbf{x}) d\mathbf{x} \\ &= \int h_{cd}(\mathbf{n}, \mathbf{x}; \theta_t) f(\mathbf{x}) d\mathbf{x}, \end{aligned} \quad (17)$$

where

$$h_{cd}(\mathbf{n}, \mathbf{x}; \theta_t) = \int w(\mathbf{n}, \mathbf{y}) h(\mathbf{y}, \mathbf{x}; \theta_t) d\mathbf{y}, \quad (18)$$

denotes the mixed-domain (continuous/discrete) point-spread function. These equations establish the linear relationship between the unknown intensity function f and the multi-frame, sampled image intensities $g_d(\mathbf{n}; \theta_t)$.

Throughout this chapter we will focus on applications for which the data collection interval for each frame is short

compared with the fluctuation time for the parameter θ_i , so that a sequence of image frames:

$$\{g_d(\mathbf{n}; k) = g_d(\mathbf{n}; \theta_k), \quad k = 1, 2, \dots, K\} \quad (19)$$

is available for detection. Each frame is recorded at the time $t = t_k$, and the blur parameter takes the value $\theta_k = \theta_{t_k}$ during the frame so that we write

$$h(\mathbf{y}, \mathbf{x}; k) = h(\mathbf{y}, \mathbf{x}; \theta_k), \quad (20)$$

and

$$h_{cd}(\mathbf{n}, \mathbf{x}; k) = h_{cd}(\mathbf{n}, \mathbf{x}; \theta_k). \quad (21)$$

2.2 Noise Models

Electromagnetic waves such as light interact with matter in a fundamentally random way, and quantum electrodynamics (QED) is the most sophisticated theory available for describing the detection of electromagnetic radiation. In most imaging applications, however, the semi-classical theory for the detection of radiation is sufficient for the development of practical and useful models. In accordance with this theory, electromagnetic energy is transported according to the classical theory of wave propagation, and the field energy is quantized only during the detection process [8].

When an optical field interacts with a photo-detector, a quantum of energy is absorbed in the form of a *photon* and the absorption of this photon gives rise to the release of an excited electron. This interaction is referred to as a photo-event, and the number of photo-events occurring within a photo-detector element during a collection interval is referred to as a photo-count. Most detectors of light record these photo-counts, and the number of photo-counts recorded during an exposure interval is a fundamentally random quantity. The utilization of this theory leads to a statistical model for image detection in which the photo-counts for each recorded frame are modeled as independent Poisson random variables, each with a conditional mean that is proportional to the sampled image intensity $g_d(\mathbf{n}; k)$ for the frame. Specifically, the expected photo-count for the n th detector during the k th frame is:

$$E[N_d(\mathbf{n}; k) | g_d(\mathbf{n}; k)] = \alpha_k g_d(\mathbf{n}; k), \quad (22)$$

where the scale factor α_k is proportional to the frame exposure time. Because the variance of a Poisson variable is equal to its mean, the image contrast (mean-squared to variance ratio) for photon noise increases linearly with the exposure time.

The data recorded by charge coupled devices (CCD) and other detectors of optical radiation are usually subject to

other forms of noise — a detailed description of image noise models is provided in Chapter 4.4. The most common for CCD cameras — *read-out* noise — is induced by the electronics used for the data acquisition. This noise is often modeled by additive, zero-mean Gaussian random variables so that the recorded data are modeled as:

$$d(\mathbf{n}; k) = N_d(\mathbf{n}; k) + v(\mathbf{n}; k), \quad (23)$$

where $v(\mathbf{n}; k)$ represents the read-out noise at the n th detector for the k th frame. The read-out noise is usually statistically independent across detectors and frames, but the variance may be different for each detector element.

3 The Multi-Frame Restoration Problem

Stated simply, the restoration problem is one of estimating the image intensity f from the blurred multi-frame data $\{d(\mathbf{n}; k), k = 1, 2, \dots, K\}$. The image intensity f is defined as a function of a continuous-domain variable, and is usually only restricted to have finite energy: $\int |f(\mathbf{x})|^2 d\mathbf{x} < \infty$. Representation of this signal cannot, in general, be accomplished through the specification of a finite set of values, and we say that f is an infinite-dimensional parameter. Estimation of f from finite data, then, is a terribly ill-conditioned problem in that there are infinitely more values to be estimated than there are data. In other words, we have a finite number of equations, but an infinite number of unknowns.

To overcome this problem, it is common to approximate the intensity function in terms of a finite-dimensional basis set:

$$f(\mathbf{x}) \simeq \sum_{\mathbf{m}} f_d(\mathbf{m}) \psi_{\mathbf{m}}(\mathbf{x}), \quad (24)$$

where the basis functions $\{\psi_{\mathbf{m}}(\mathbf{x})\}$ are selected in a manner that is appropriate for the application. Expression of the object function on a predetermined grid of pixels, for example, might require $\psi_{\mathbf{m}}(\mathbf{x})$ to be an indicator function that denotes the location and spatial support of the m th pixel:

$$\psi_{\mathbf{m}}(\mathbf{x}) = \begin{cases} 1 & \mathbf{x} \text{ is in the spatial support of the } m\text{th} \\ & \text{detector element} \\ 0 & \mathbf{x} \text{ is not in the spatial support of the } m\text{th} \\ & \text{detector element} \end{cases} \quad (25)$$

Alternatively, the basis functions might be selected as two-dimensional impulses co-located with the center of each pixel. Other basis sets are possible, and a clever choice here can have a great effect on estimator performance.

Using a basis as described in (24) results in the following approximation to the imaging equation:

$$\begin{aligned}
 g_d(\mathbf{n}; k) &= \int h_{cd}(\mathbf{n}, \mathbf{x}; k) f(\mathbf{x}) d\mathbf{x} \\
 &\simeq \int h_{cd}(\mathbf{n}, \mathbf{x}; k) \sum_{\mathbf{m}} f_d(\mathbf{m}) \psi_{\mathbf{m}}(\mathbf{x}) d\mathbf{x} \\
 &= \sum_{\mathbf{m}} \left[\int h_{cd}(\mathbf{n}, \mathbf{x}; k) \psi_{\mathbf{m}}(\mathbf{x}) d\mathbf{x} \right] f_d(\mathbf{m}) \\
 &= \sum_{\mathbf{m}} h_d(\mathbf{n}, \mathbf{m}; k) f_d(\mathbf{m}), \quad k = 1, 2, \dots, K, \quad (26)
 \end{aligned}$$

where

$$h_d(\mathbf{n}, \mathbf{m}; k) = \int h_{cd}(\mathbf{n}, \mathbf{x}; k) \psi_{\mathbf{m}}(\mathbf{x}) d\mathbf{x} \quad (27)$$

is the discrete-domain impulse response for the k th frame. This impulse response (or point-spread function) defines a linear relationship between the discrete-domain images $\{g_d(\mathbf{n}; k)\}$ and the discrete-domain intensity $f_d(\mathbf{m})$. For shift-invariant applications, h_d is a function of only the difference $\mathbf{n} - \mathbf{m}$. With a little thought on notation, the discrete-domain imaging equations can be written in matrix-vector form as

$$\mathbf{g}_d(k) = \mathbf{H}_d(k) \mathbf{f}_d, \quad k = 1, 2, \dots, K, \quad (28)$$

and when the point-spread functions are shift-invariant, the measurement matrices $\{\mathbf{H}_d(k), k = 1, 2, \dots, K\}$ have equal elements along their diagonals and are said to have *Toeplitz* structure. This structure can greatly simplify restoration problems because efficient methods exist for the solution of linear equations with Toeplitz structure. One potential advantage of multi-frame restoration methods arises when the eigensystems for the measurement matrices are sufficiently different. In this situation, each image frame records different information about the object, and the system of multi-frame measurements can be used to estimate more detail about the object than can a single image frame.

3.1 Restoration as an Optimization Problem

In this section we focus on restoration problems for which the point-spread parameters $\{\theta_k\}$ are well-known or easily determined. In the following section we will address the challenges that are presented when these parameters must be identified from the measured data.

Statistical inference problems such as those encountered in multi-frame image restoration are frequently classified as ill-posed problems [9], and, because of this, *regularization* methods play an important role in the estimation process. (See Chapter 3.11 for an excellent overview of the significance of regularization methods for image recovery.) An

image-restoration problem is ill posed if it is not well posed, and a problem is well posed in the classical sense of Hadamard if it has a unique solution and the solution varies continuously with the data. Multi-frame image restoration problems that are formulated on infinite-dimensional parameter spaces are almost always ill posed, and their ill-posed nature is usually due to the discontinuity of the solution. That is, very small changes in the data (measurement noise) lead to very large changes in the solution. Problems that are formulated on finite-dimensional spaces (as ours is here) are frequently well-posed in the classical sense — they have a unique solution and the solution is continuous in the data. However, these problems are usually ill conditioned or badly behaved and are frequently classified as ill posed even though they are technically well posed.

For problems that are ill posed or practically ill posed, the original problem's solution is often replaced by the solution to a well-posed (or well-behaved) problem. This process is referred to as regularization, and the basic idea is to change the problem in a manner such that the solution is still meaningful but no longer badly behaved [9]. The consequence for multi-frame restoration problems is that we do not seek to match the measured data perfectly. Instead, we settle for a more stable — but inherently biased — image estimate.

Most approaches to regularized image-restoration are induced through attempts to solve an optimization problem of the following form:

$$\hat{\mathbf{f}}_d = \arg \min_{\mathbf{f}_d \in \mathcal{F}} \{D(\mathbf{g}_d, \mathbf{d}) + \gamma \psi(\mathbf{f}_d)\}, \quad (29)$$

where $D(\mathbf{g}_d, \mathbf{d})$ is a discrepancy measure between the estimated image intensities $\{g_d(\mathbf{n}; k), k = 1, 2, \dots, K\}$ and the measured data $\{d(\mathbf{n}; k), k = 1, 2, \dots, K\}$, $\psi(\mathbf{f}_d)$ is a penalty (or prior) function that penalizes undesirable attributes of the object estimate $\mathbf{f}_d(\mathbf{m})$ (or rewards desirable ones), γ is a scale factor that determines the degree to which the penalty influences the estimate, and \mathcal{F} is a constraint set of allowable object estimates. In (29), *arg min* is a notation that tells us to return the value of \mathbf{f}_d within the constraint set \mathcal{F} that minimizes the quantity within the braces. This should not be confused with the actual minimum that the quantity attains. For instance, the minimum of $(x - 3)^2$ over all real numbers x is 0, but the value of x at which this minimum is attained is 3. Therefore, 3 is the *arg min* of $(x - 3)^2$. Methods that are covered by this general framework include:

- **Maximum-Likelihood Estimation:** For maximum-likelihood estimation the penalty is not used ($\gamma = 0$), the constraint set is typically the set of nonnegative functions $\mathcal{F} = \{\mathbf{f}_d : \mathbf{f}_d \geq 0\}$, and the discrepancy measure is induced by the statistical model that is used for the data collection process. Discrepancy measures that result

from various noise models are illustrated in the following examples.

Example 3.1 (Maximum-Likelihood for Gaussian Noise) When the measured data are corrupted only by additive, independent Gaussian noise of variance σ^2 , the data are modeled as

$$d(\mathbf{n}; k) = g_d(\mathbf{n}; k) + v(\mathbf{n}; k), \quad (30)$$

and the log-likelihood function is of the form

$$L(d; g_d) = -\frac{1}{2\sigma^2} \sum_k \sum_n [d(\mathbf{n}; k) - g_d(\mathbf{n}; k)]^2. \quad (31)$$

The discrepancy measure can then be selected as

$$D(g_d, d) = \sum_k \sum_n [d(\mathbf{n}; k) - g_d(\mathbf{n}; k)]^2, \quad (32)$$

where the scale factor $1/2\sigma^2$ is omitted without affecting the optimization.

Example 3.2 (Maximum-Likelihood for Poisson Noise) When the measured data are corrupted only by Poisson (photon) noise, the log-likelihood function is of the form

$$L(d; g_d) = -\sum_k \sum_n \alpha_k g_d(\mathbf{n}; k) + \sum_k \sum_n d(\mathbf{n}; k) \ln \alpha_k g_d(\mathbf{n}; k), \quad (33)$$

and the discrepancy measure is selected as

$$D(g_d, d) = \sum_k \sum_n \alpha_k g_d(\mathbf{n}; k) - \sum_k \sum_n d(\mathbf{n}; k) \ln \alpha_k g_d(\mathbf{n}; k). \quad (34)$$

Example 3.3 (Maximum-Likelihood for Poisson and Gaussian Noise) When the measured data are corrupted by both Poisson (photon) noise and additive Gaussian (read-out) noise as in (23), then the likelihood has a complicated form involving an infinite summation [10]. When the variance for the Gaussian noise is the same for all detector elements and sufficiently large (greater than 50 or so), however, the modified data:

$$\tilde{d}(\mathbf{n}; k) = d(\mathbf{n}; k) + \sigma^2, \quad (35)$$

have an approximate log-likelihood of the form [10]:

$$L(d; g_d) = -\sum_k \sum_n \{\alpha_k g_d(\mathbf{n}; k) + \sigma^2\} + \sum_k \sum_n \tilde{d}(\mathbf{n}; k) \ln \{\alpha_k g_d(\mathbf{n}; k) + \sigma^2\}. \quad (36)$$

The discrepancy measure is then

$$D(g_d, d) = \sum_k \sum_n \{\alpha_k g_d(\mathbf{n}; k) + \sigma^2\} - \sum_k \sum_n \tilde{d}(\mathbf{n}; k) \ln \{\alpha_k g_d(\mathbf{n}; k) + \sigma^2\}. \quad (37)$$

- **Sieve-Constrained Maximum-Likelihood Estimation:** For sieve-constrained maximum-likelihood estimation [11], the discrepancy measure is again induced by the statistical model that is used for the data collection process and the penalty is not used ($\gamma = 0$). However, the constraint set is selected to be a “smooth” subset of nonnegative functions. A Gaussian kernel sieve [11], for example, is defined as:

$$\mathcal{F} = \left\{ f_d : f_d(\mathbf{m}) = \sum_p \alpha(\mathbf{p}) \frac{1}{\sqrt{2\pi a}} e^{-\frac{(\mathbf{p}-\mathbf{m})^2}{2a}}, \quad \alpha(\mathbf{p}) \geq 0 \right\}, \quad (38)$$

where the parameter a determines the width of the Gaussian kernel and the “smoothness” of the sieve. Whereas some theory is available to guide the selection of a , for most applications the selection of this parameter is part of the *art* of performing sieve-constrained estimation.

- **Penalized Maximum-Likelihood Estimation:** For penalized maximum-likelihood estimation, the discrepancy measure is induced by the statistical model that is used for the data collection, and the constraint set is typically the set of nonnegative functions. However, the function ψ is chosen to penalize undesirable properties of the object estimate. Commonly used penalties include:

The Weighted Quadratic Roughness Penalty:

$$\psi(f_d) = \sum_{\mathbf{m}} \sum_{\mathbf{m}' \in \mathcal{N}_{\mathbf{m}}} w(\mathbf{m}, \mathbf{m}') |f_d(\mathbf{m}) - f_d(\mathbf{m}')|^2, \quad (39)$$

where $\mathcal{N}_{\mathbf{m}}$ denotes a neighborhood about the \mathbf{m} th pixel and $w(\mathbf{m}, \mathbf{m}')$ is a nonnegative weighting function.

The Divergence Penalty:

$$\psi(f_d) = \sum_{\mathbf{m}} f_d(\mathbf{m}) \ln f_d(\mathbf{m}) - \sum_{\mathbf{m}} f_d(\mathbf{m}) \sum_{\mathbf{m}' \in \mathcal{N}_{\mathbf{m}}} \ln f_d(\mathbf{m}'), \quad (40)$$

where $\mathcal{N}_{\mathbf{m}}$ is again a neighborhood about the \mathbf{m} th pixel.

Many other roughness penalties are possible [12], and the proper choice can depend largely on the application. As with the selection of the sieve parameter for sieve-constrained estimation, selection of the parameter γ for a particular

application is part of the *art* of using penalized maximum-likelihood methods. When γ is selected to be too small, the estimates usually have fine resolution but exhibit too much roughness; when γ is selected to be too large, the estimates usually exhibit little roughness, but at the expense of resolution. Asymptotic theories are available to guide the selection of γ , but in most cases experience is used to select its value so that the trade-off between smoothness and resolution is best managed.

- **Maximum *a Posteriori* Estimation:** For maximum *a posteriori* (MAP) estimation, the discrepancy measure is induced by the statistical model for the data collection, and the constraint set is typically the set of nonnegative functions. However, the penalty term $\psi(f_d)$ and scale factor γ are induced by a prior statistical model for the unknown object intensity. MAP methods are mathematically, but not always philosophically, equivalent to penalty methods. Markov random fields (MRF) are commonly used for image priors, and, within this framework, Bouman and Sauer [13] have proposed and investigated the use of a generalized Gauss–Markov random field (GGMRF) model for images:

$$\psi(f_d) = \sum_{\mathbf{m}} a(\mathbf{m}) |f_d(\mathbf{m})|^p + \sum_{\mathbf{m}} \sum_{\mathbf{m}' \in \mathcal{N}_{\mathbf{m}}} b(\mathbf{m}, \mathbf{m}') |f_d(\mathbf{m}) - f_d(\mathbf{m}')|^p, \quad (41)$$

$$\hat{f}_d = \arg \min_{f_d} \left\{ \sum_k \sum_{\mathbf{n}} [d(\mathbf{n}; k) - g_d(\mathbf{n}; k)]^2 + \gamma \sum_s \left[\sum_{\mathbf{m}} C(s, \mathbf{m}) f_d(\mathbf{m}) \right]^2 \right\}, \quad (44)$$

where $p \in [1, 2]$, and $a(\mathbf{m})$ and $b(\mathbf{m}, \mathbf{m}')$ are nonnegative parameters. A detailed discussion of the effect of p , a , and b on estimator performance is provided in ref. [13].

- **Regularized Least Squares Estimation:** For regularized least squares estimation, the discrepancy measure is selected as:

$$D(g_d, d) = \sum_k \sum_{\mathbf{n}} [g_d(\mathbf{n}; k) - d(\mathbf{n}; k)]^2, \quad (42)$$

the constraint set is typically the set of nonnegative functions, and the penalty is selected and used as discussed for penalized maximum-likelihood estimation. For additive, white Gaussian noise, the regularized least squares and penalized maximum-likelihood methods are mathematically equivalent.

- **Minimum I-Divergence Estimation:** For problems involving nonnegative image measurements, the

I-Divergence has also received attention as a discrepancy measure:

$$D(g_d, d) = \sum_k \sum_{\mathbf{n}} [g_d(\mathbf{n}; k) - d(\mathbf{n}; k)] - \sum_k \sum_{\mathbf{n}} d(\mathbf{n}; k) \ln \frac{g_d(\mathbf{n}; k)}{d(\mathbf{n}; k)}. \quad (43)$$

For problems in which the noise is Poisson, the minimum I-divergence and maximum-likelihood methods are mathematically equivalent.

After selecting an appropriate estimation methodology, multi-frame image restoration — as we have posed the problem here — is a problem of constrained optimization. For most situations this optimization must be performed numerically, but in some cases a direct-form linear solution can be obtained. In these situations, however, the physical constraint that the intensity function f must be nonnegative is usually ignored.

3.2 Linear Methods

Linear methods for solving multi-frame restoration problems are usually derived as solutions to the regularized least-squares problem:

where C is called the regularizing operator. A common choice for this operator is the two-dimensional Laplacian:

$$C(s, \mathbf{m}) = \begin{cases} 1 & s = \mathbf{m} \\ -1/4 & s = \mathbf{m} + (0, 1) \\ -1/4 & s = \mathbf{m} + (0, -1) \\ -1/4 & s = \mathbf{m} + (1, 0) \\ -1/4 & s = \mathbf{m} + (-1, 0) \\ 0 & \text{otherwise} \end{cases}, \quad (45)$$

but other operators can be used. In matrix-vector notation, the regularized least-squares optimization problem can be reposed as:

$$\hat{f}_d = \arg \min_{f_d} \left\{ \sum_k \|d(k) - H(k) f_d\|^2 + \gamma \|C f_d\|^2 \right\}, \quad (46)$$

with the minimum-norm solution \hat{f}_d satisfying:

$$\sum_k \mathbf{H}^T(k) \mathbf{d}(k) = \left(\sum_k \mathbf{H}^T(k) \mathbf{H}(k) + \gamma \mathbf{C}^T \mathbf{C} \right) \hat{f}_d, \quad (47)$$

or

$$\hat{f}_d = \left(\sum_k \mathbf{H}^T(k) \mathbf{H}(k) + \gamma \mathbf{C}^T \mathbf{C} \right)^{-1} \sum_k \mathbf{H}^T(k) \mathbf{d}(k), \quad (48)$$

when the inverse exists for $(\sum_k \mathbf{H}^T(k) \mathbf{H}(k) + \gamma \mathbf{C}^T \mathbf{C})$. A key to the derivation of a linear solution to (46) is the absence of a nonnegativity constraint. If the solution is constrained to be nonnegative, then a linear solution will not exist in general. Solutions for problems in which the nonnegativity constraint must be satisfied generally require iterative, nonlinear processing. Furthermore, because the processing required to solve (47) and (48) can be prohibitive, iterative methods can be required even when attempting to solve the unconstrained problem.

3.3 Nonlinear (Iterative) Methods

The presence of a nonnegativity constraint or the use of non-quadratic discrepancy measures and penalties will, in general, prohibit the derivation of a closed-form, linear solution to the multi-frame restoration problem. Instead, iterative methods are needed. Basic descent methods, coordinate descent methods, conjugate direction methods, and quasi-Newton methods can all be applied to solve the general optimization problem:

$$\hat{f}_d = \arg \min_{f_d \in \mathcal{F}} \{D(g_d, d) + \gamma \psi(f_d)\}, \quad (49)$$

and the most appropriate method will, in general, depend on the application. For problems in which the discrepancy measure $D(g_d, d)$ is induced by a statistical procedure such as maximum-likelihood or MAP estimation, another class of optimization methods can also be applied. These are derived via the expectation-maximization (EM) procedure, the generalized EM procedure, or the space alternating generalized EM (SAGE) procedure [14]. For problems in incoherent imaging and statistical tomography [15], the SAGE procedure leads to methods that are similar in form to coordinate descent optimization [16], and both methods lead to highly efficient optimization procedures.

4 Nuisance Parameters and Blind Restoration

In the previous section, we addressed the restoration problem for situations in which the parameters $\{\theta_k\}$ that characterize

the point-spread functions are well-known or easily predicted. This is not the case for applications such as uncontrolled microscanning and imaging through turbulence, and in these situations the unknown parameters must be eliminated or estimated. Estimation of these parameters often leads to one of the following optimization problems:

$$\hat{f}_d = \arg \min_{f_d \in \mathcal{F}} \{D(g_d, d; \hat{\theta}(f_d)) + \gamma \psi(f_d)\}, \quad (50)$$

$$\hat{\theta}(f_d) = \arg \min_{\theta \in \Theta} E(f_d, d; \theta),$$

or

$$(\hat{f}_d, \hat{\theta}) = \arg \min_{f_d \in \mathcal{F}} \{D(g_d, d; \theta) + \gamma \psi(f_d) + \beta \Upsilon(\theta)\}, \quad (51)$$

where the discrepancy measure D now shows an explicit dependence on the unknown parameters $\theta = \{\theta_k\}$. For the first approach (50), we fix the unknown intensity f_d and estimate θ by minimizing some cost functional E over the constraint set Θ . The cost functional may be induced by estimation-theoretic principles, or it may be motivated through heuristic arguments. The resulting estimate for θ , which may be a function of the unknown intensity f_d , is then used in the original discrepancy measure D , and an estimator for f_d is determined. For the second approach (51), the unknown parameters θ and intensity f_d are jointly estimated by minimizing a cost functional containing a discrepancy measure D , an intensity penalty ϕ and a parameter penalty Υ . Determination of the discrepancy measure and penalty functionals can be approached in a manner similar to that discussed in the previous section.

Many methods have been proposed for solving multi-frame blind restoration problems, and each has been tailored for specific blur models. For microscanning applications with undersampled detectors, the blur models are often as in (14) with frame-to-frame translations and rotations of the diffraction-limited point-spread [1]. For ground-based imaging of astronomical and space objects, the blur models are usually as in (10), with phase aberrations distributed across the system's aperture [3]. Another class of solutions has addressed problems for which the discrete-domain point-spreads are modeled as two-dimensional finite impulse response (FIR) filters, for which 'perfect' or 'exact' methods can be extended from methods developed for one-dimensional applications [17, 18].

The successful application of a few methods developed for real-world imaging problems is illustrated in the following section.

5 Applications

We conclude this chapter by presenting an overview of four applications of multi-frame blind restoration.

5.1 Fine-Resolution Imaging from Undersampled Image Sequences

For problems in which an image is undersampled by the system's detector array, multi-frame restoration methods can be used to obtain a fine-resolution object estimate provided that a sequence of translated (or microscanned) images is obtained. An example considered by Hardie et al. [1] concerns image formation with a forward-looking infrared (FLIR) imaging system. This system's continuous-domain point-spread function due to diffraction is modeled as:

$$h(\mathbf{y}) = \left| \int A(\mathbf{u}) e^{-j\frac{2\pi}{\lambda f} \mathbf{u} \cdot \mathbf{y}} d\mathbf{u} \right|^2, \quad (52)$$

where $A(\mathbf{u})$ denotes the system's pupil function as determined by the physical dimensions of the camera's lens, λ is the operational wavelength, and f is the system focal length. Accordingly, the continuous-domain intensity due only to diffraction is modeled as

$$g_c(\mathbf{y}) = \int h(\mathbf{y} - \mathbf{x}) f(\mathbf{x}) d\mathbf{x}. \quad (53)$$

For a circular lens of diameter D , the highest spacial frequency present in the continuous-domain image is $D/(\lambda f)$, so that critical sampling of the image is obtained on a grid whose spacing is $\lambda f/(2D)$.

The sampling operator for FLIR cameras is typically of the form

$$w(\mathbf{n}, \mathbf{y}) = \begin{cases} 1 & \mathbf{y} \in \mathcal{Y}_n \\ 0 & \text{otherwise} \end{cases}, \quad (54)$$

where \mathcal{Y}_n is a rectangular neighborhood around the center of the n th detector element \mathbf{y}_n . For a circular aperture of radius D , if the spacing between detector elements is greater than $\lambda f/(2D)$, as is often the case for current FLIR systems, then the image data will be undersampled and the full resolving power of the system will not be utilized. Frame-to-frame motion or camera jitter in conjunction with multi-frame image restoration methods can, however, be used to restore resolution to an undersampled system.

Frame-to-frame motion or camera jitter, in the form of translations and rotations, can be modeled by modifying the

continuous-domain imaging equation according to

$$\begin{aligned} g_c(\mathbf{y}; \theta_k) &= \int h(\mathbf{y} - \mathbf{x}) f[\mathbf{A}(\phi_k)\mathbf{x} - \Delta_k] d\mathbf{x} \\ &= \int h[\mathbf{y} - \mathbf{A}^{-1}(\phi_k)(\mathbf{x} + \Delta_k)] f(\mathbf{x}) d\mathbf{x} \\ &= \int h(\mathbf{y}, \mathbf{x}; \theta_k) f(\mathbf{x}) d\mathbf{x} \end{aligned} \quad (55)$$

where Δ_k denotes the two-dimensional translation, and

$$\mathbf{A}(\phi_k) = \begin{bmatrix} \cos(\phi_k) & -\sin(\phi_k) \\ \sin(\phi_k) & \cos(\phi_k) \end{bmatrix}, \quad (56)$$

is the rotation matrix (at angle ϕ_k) associated with the k th frame. These parameters, $\{\theta_k = (\Delta_k, \phi_k)\}$, are often unknown at the time of data collection, and the accurate estimation of their values is essential for fine-resolution enhancement of multi-frame FLIR imagery.

Hardie et al. [1] have addressed this problem for an application using a FLIR camera with an Amber AE-4 infrared focal plane array (FPA). The nominal wavelength for this system is $\lambda = 4 \mu\text{m}$, and the aperture diameter is $D = 100 \text{ mm}$. With a focal length of 300 mm, the required sample spacing for critical sampling is $\lambda f/(2D) = 6 \mu\text{m}$; however, the detector spacing for the Amber FPA is $50 \mu\text{m}$ with integration neighborhoods that are $40 \mu\text{m}$ square. This results in undersampling by a factor of 8.33.

Using an object expansion of the form:

$$f(\mathbf{x}) = \sum_{\mathbf{m}} f_d(\mathbf{m}) \psi_{\mathbf{m}}(\mathbf{x}), \quad (57)$$

where the basis functions $\{\psi_{\mathbf{m}}(\mathbf{x})\}$ represent two-dimensional square functions with spatial support that is 5 times smaller than the detector elements ($10 \mu\text{m} \times 10 \mu\text{m}$), Hardie et al. used a preprocessing registration method to estimate the frame-to-frame rotations and shifts $\{\theta_k = (\mathbf{A}(\phi_k), \Delta_k)\}$ followed by a regularized least-squares method to restore a fine-resolution scene estimate from a multi-frame sequence of noisy microscanned images. This is the two-step procedure as described by (50). The regularization operator was the discretized Laplacian from (45), and the smoothing parameter γ was tuned in a heuristic manner. A conjugate-gradient approach, based on the Fletcher-Reeves method, was used to solve the multi-frame optimization problem. A typical image frame is displayed in Fig. 7-(a), showing a FLIR image of buildings and roads in the Dayton, Ohio area.² A multi-frame image restoration obtained from 20 such frames, each with

²These data were collected courtesy of the Infrared Threat Warning Laboratory, Threat Detection Branch at Wright Laboratory (WL/AAJP).

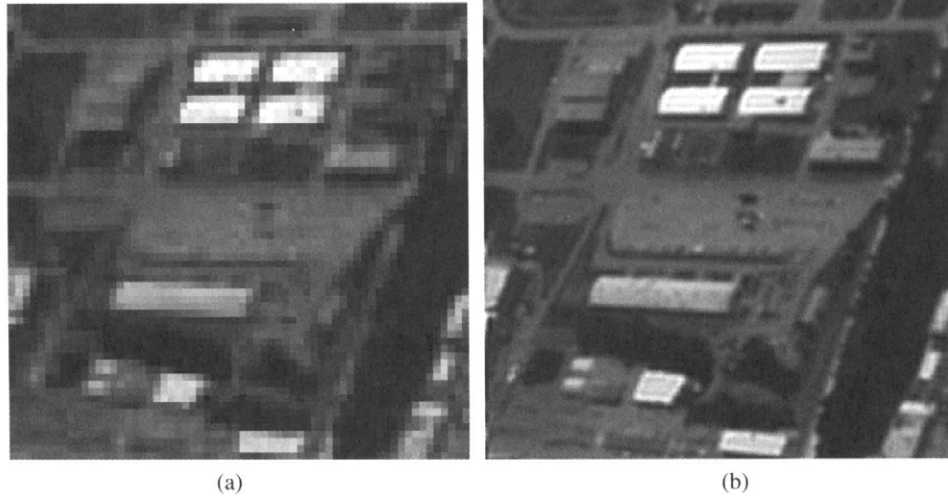


FIGURE 7 Demonstration of multi-frame image restoration for undersampled FLIR images: (a) an undersampled image frame from the FLIR imagery; (b) the restored image by processing 20 similar undersampled frames.

unknown translations and rotations, is shown in Fig. 7(b). Clearly, resolution has been improved in the imagery.

5.2 Ground-based Imaging through Atmospheric Turbulence

The distorting effects of atmospheric turbulence give rise to continuous-domain point-spread functions of the form:

$$h(\mathbf{y}; k) = \left| \int A(\mathbf{u}) e^{j\theta_k(\mathbf{u})} e^{-j\frac{2\pi}{\lambda f} \mathbf{u} \cdot \mathbf{y}} d\mathbf{y} \right|^2, \quad (58)$$

where θ_k represents the turbulence-induced aberrations for the k th frame. The discrete-domain point-spread function is then of the form

$$\begin{aligned} h_d(\mathbf{n}, \mathbf{m}; k) &= \int h_{cd}(\mathbf{n}, \mathbf{x}; k) \phi_{\mathbf{m}}(\mathbf{x}) d\mathbf{x} \\ &= \iint w(\mathbf{n}, \mathbf{y}) h(\mathbf{y} - \mathbf{x}; k) \psi_{\mathbf{m}}(\mathbf{x}) d\mathbf{y} d\mathbf{x}, \end{aligned} \quad (59)$$

and, if the spatial support for the detector elements $w(\mathbf{n}, \mathbf{y})$ and basis functions $\psi_{\mathbf{m}}(\mathbf{x})$ are sufficiently small, then the discrete-domain point spread can be reasonable approximated as:

$$h_d(\mathbf{n}, \mathbf{m}; k) \simeq h(\mathbf{y}_{\mathbf{n}} - \mathbf{x}_{\mathbf{m}}; k), \quad (60)$$

where $\mathbf{y}_{\mathbf{n}}$ is the spatial location of the \mathbf{n} th detector element and $\mathbf{x}_{\mathbf{m}}$ is the spatial location of the \mathbf{m} th object pixel. If the detector elements and object pixels are furthermore on the same grid ($\Delta_{\mathbf{x}} = \Delta_{\mathbf{y}}$), then the discrete-domain point spread can be further approximated as:

$$h_d(\mathbf{n}, \mathbf{m}; k) \simeq \left| \sum_{\mathbf{l}} A(\Delta_{\mathbf{u}} \mathbf{l}) e^{j\theta_k(\Delta_{\mathbf{u}} \mathbf{l})} e^{-j\frac{2\pi}{\lambda f} \Delta_{\mathbf{u}} \Delta_{\mathbf{x}} \mathbf{l} \cdot (\mathbf{n} - \mathbf{m})} \right|^2, \quad (61)$$

where $\Delta_{\mathbf{u}}$ is the pupil-plane discretization grid spacing. If the aperture and image planes are discretized on a grid of size $N \times N$ (a square grid with $N = M$) and if $\Delta_{\mathbf{u}} \Delta_{\mathbf{x}} / (\lambda f) = 1/N$, then the discrete-domain point spread can be approximated by the space-invariant function:

$$h_d(\mathbf{m}; k) \simeq \left| \sum_{\mathbf{l}} A(\mathbf{l}) e^{j\theta_k(\mathbf{l})} e^{-j\frac{2\pi}{N} \mathbf{l} \cdot \mathbf{m}} \right|^2, \quad (62)$$

where $A(\mathbf{l}) = A(\Delta_{\mathbf{u}} \mathbf{l})$ and $\theta_k(\mathbf{l}) = \theta_k(\Delta_{\mathbf{u}} \mathbf{l})$. Using these approximations, the discrete-domain point spread can be easily and efficiently computed via the fast Fourier transform (FFT) algorithm. The discrete-domain imaging equations are then:

$$g_d(\mathbf{n}; k) = \sum_{\mathbf{m}} h_d(\mathbf{n} - \mathbf{m}; k) f_d(\mathbf{m}), \quad (63)$$

and the joint estimation of the unknown object and the turbulence parameters in the presence of Poisson (photon) noise can be accomplished by solving the following maximum-likelihood problem:

$$\begin{aligned} (\hat{f}_d, \hat{\theta}) &= \arg \min_{f_d \in \mathcal{F}, \theta \in \Theta} \\ &\times \left\{ \sum_{\mathbf{k}} \sum_{\mathbf{n}} g_d(\mathbf{n}; k) - \sum_{\mathbf{k}} \sum_{\mathbf{n}} d(\mathbf{n}; k) \ln g_d(\mathbf{n}; k) \right\}. \end{aligned} \quad (64)$$

Numeric methods that include extensions to problems involving Gaussian (read-out) noise and nonuniform detector gain and bias are presented in refs. [3, 19, 20].

The use of this method on telescope data is illustrated in Fig. 8. As illustrated in the figure, several frames of the rear portion of the Space Shuttle Discovery were acquired in 1998

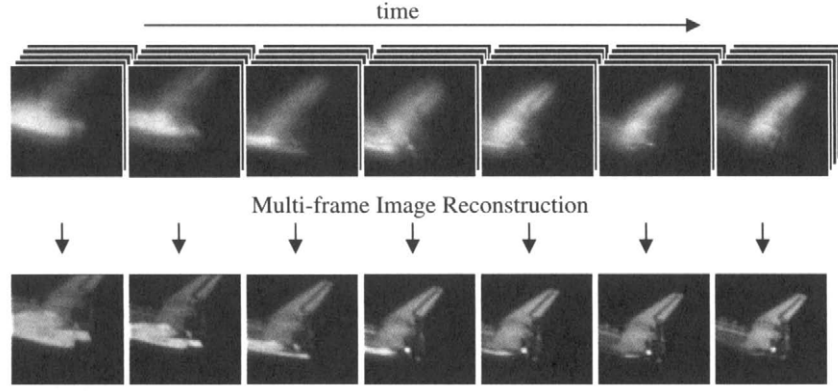


FIGURE 8 Multi-frame imagery and restored image estimates of the Space Shuttle Discovery as acquired by a 1.6 m telescope at the Air Force Maui Space Surveillance Site.

by using a 1.6 m telescope at the Air Force Maui Space Surveillance Site. The flight crew for this particular shuttle flight included the national hero John Glenn, and, shortly after launch, video showed that the compartment cover for the drag chute had fallen off the shuttle. Because no spacewalk activities were planned, visual inspection was possible only by using ground-based telescopes. Data were subsequently acquired using an Air Force telescope at a nominal wavelength of 880 nm with a field-of-view for each exposure equal to 6 seconds of arc. The image data were partitioned into segments of between 10 and 25 frames, and maximum-likelihood image estimates were obtained. Whereas the 1.6 m telescope did not allow for resolution sufficient to fully assess potential damage, diffraction-limited images were obtained through turbulence with a ground-based telescope.

5.3 Ground-based Solar Imaging with Phase Diversity

Phase-diverse speckle (PDS) is a *measurement* and processing method for the simultaneous estimation of an object and the atmospheric phase aberrations from multi-frame imagery acquired in the presence of turbulence-induced aberrations. By modifying a telescope to simultaneously record both an in-focus and out-of-focus image for each exposure frame, the phase-diverse speckle method records a sequence of discrete-domain images that are formed according to:

$$g_{c1}(\mathbf{n}; k) = \sum_{\mathbf{m}} h_d(\mathbf{n} - \mathbf{m}; k) f_d(\mathbf{m}) \quad (65)$$

and

$$g_{c2}(\mathbf{n}; k) = \sum_{\mathbf{m}} h_d(\mathbf{n} - \mathbf{m}; k, \theta_{df}) f_d(\mathbf{m}), \quad (66)$$

where $h_d(\mathbf{m}; k)$ is the point-spread function for turbulence and diffraction (parameterized by the turbulence-induced aberration parameters θ_k for the k th frame as defined in (62),

and $h_d(\mathbf{m}; k, \theta_{df})$ is the out-of-focus point-spread function for the same frame. The additional aberration due to the known defocus error θ_{df} is usually well modeled as a quadratic function

$$\theta_{df}(\mathbf{l}) = a \|\mathbf{l}\|^2, \quad (67)$$

so that:

$$h_d(\mathbf{m}; k, \theta_{df}) = \left| \sum_{\mathbf{l}} A(\mathbf{l}) e^{j[\theta_k(\mathbf{l}) + a \|\mathbf{l}\|^2]} e^{-j \frac{2\pi}{\lambda} \mathbf{l} \cdot \mathbf{m}} \right|^2. \quad (68)$$

For Poisson (photon) noise, the maximum-likelihood estimation of the object and aberrations is accomplished by solving the following optimization problem:

$$\begin{aligned} (\hat{f}_d, \hat{\theta}) = \arg \min_{f_d \in \mathcal{F}, \theta \in \Theta} & \\ \times \left\{ \sum_k \sum_{i=1}^2 \sum_{\mathbf{n}} g_{di}(\mathbf{n}; k) \right. & \\ \left. - \sum_k \sum_{i=1}^2 \sum_{\mathbf{n}} d(\mathbf{n}; k, i) \ln g_{di}(\mathbf{n}; k) \right\}, & \quad (69) \end{aligned}$$

where $d(\mathbf{n}; k, 1)$ and $d(\mathbf{n}; k, 2)$ are the in-focus and out-of-focus images for the k th frame, respectively. Although the formation of two images for each frame generally leads to less light and an increased noise level in each recorded image, the addition of the defocused diversity channel can result in significant improvements in the ability to restore fine-resolution imagery from turbulence degraded imagery.

Paxman, Seldin, et al. [21] have applied this method with great success to a problem in solar imaging by using a quasi-Newton method for the optimization of (69). Within their estimation procedure, they have modified the measurement model to account for nonuniform detector gain and bias, included a Gaussian-kernel sieve constraint for the object, as

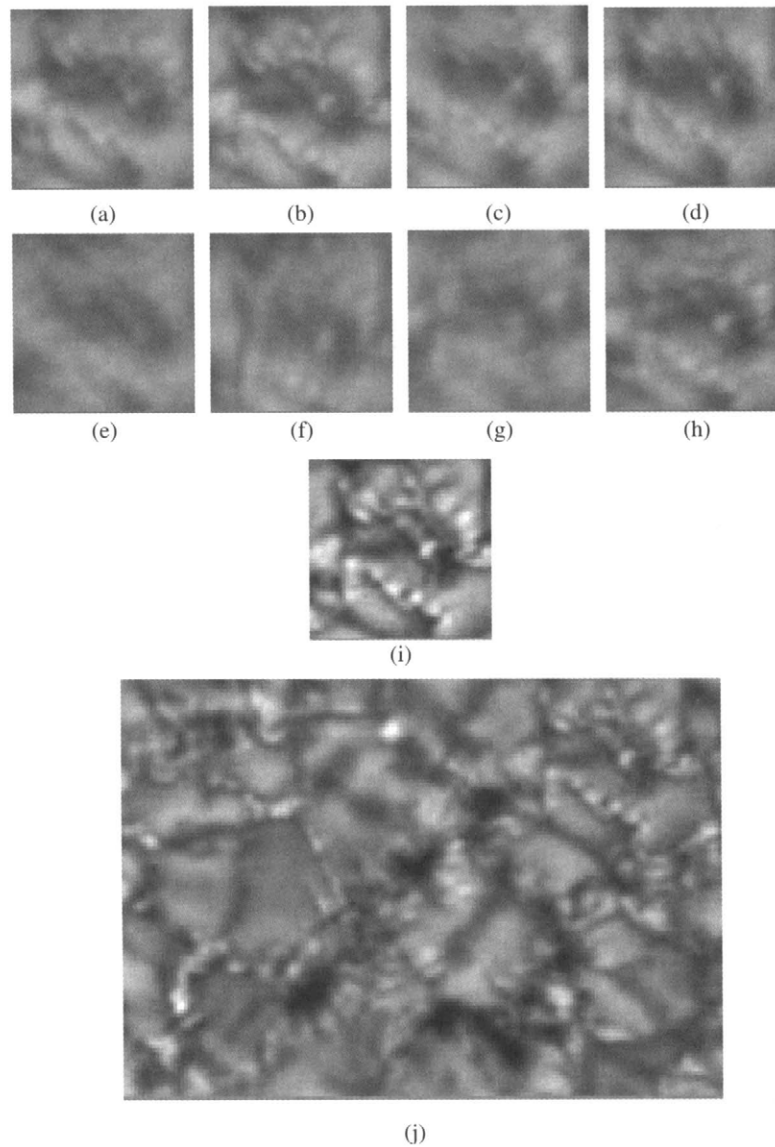


FIGURE 9 Phase diverse speckle: (a)–(d) in-focus image frames; (e)–(h) de-focus image frames; (i) restoration from 10 in-focus and de-focus image frames; (j) large field-of-view obtained from 35 small field-of-view restorations on a 5×7 grid.

in (38), and incorporated a polynomial expansion for the phase aberrations:

$$\Theta = \left\{ \theta_k(\mathbf{l}) = \sum_i a_{ki} z_i(\mathbf{l}/R), \quad k = 1, 2, \dots, K \right\}, \quad (70)$$

where R is the radius of the telescope's aperture, and the polynomial functions $\{z_i(\mathbf{l})\}$ are the circle polynomials of Zernike, which are orthonormal over the interior of a unit circle. These polynomials have found widespread use in optics because they represent common aberration modes such as defocus, coma, and spherical aberration, and because they form a good approximation to the Karhunen–Loeve

expansion for atmospheric aberrations that obey Kolmogorov statistics [8].

The top row of Fig. 9 shows four in-focus image frames that were acquired by Dr. Christoph Keller using a 76 cm vacuum tower telescope at the National Solar Observatory on Sacramento Peak, NM. Many processes in the solar atmosphere have typical spatial scales that are much smaller than the resolution of these blurred images, and because of this important solar features cannot be observed without some form of image restoration. The second row of Fig. 9 shows the corresponding out-of-focus image frames that were acquired for use with the phase diverse speckle method. Using in-focus and de-focused image pairs from 10 frames, Paxman and Seldin obtained the restored image shown in

Fig. 9(i). The restored image for this field-of-view was blended with 34 others on a 5×7 grid across the solar surface to create the large field-of-view restoration shown in Fig. 9(j). By using the phase diversity method, the resolution of the large field-of-view restoration is now sufficient to perform meaningful inferences about solar processes.

Acknowledgments

Data acquisition for the Space Shuttle Discovery example in Section 5.2 was coordinated by Dave Tyler (then with the Albuquerque High Performance Computing Center) and the processing was implemented by John Seldin (then with Veridian and ERIM International).

References

- [1] R. C. Hardie, K. J. Barnard, J. G. Bogner, E. E. Armstrong, and E. A. Watson. "High-resolution image reconstruction from a sequence of rotated and translated frames and its application to an infrared imaging system." *Opt. Eng.*, 37(1):247–260, 1998.
- [2] R. R. Schultz and R. L. Stevenson. "Extraction of high-resolution frames from video sequences." *IEEE Trans. Image Processing*, 5:996–1011, 1996.
- [3] T. J. Schulz. "Multi-frame blind deconvolution of astronomical images." *J. Opt. Soc. Am. A*, 10:1064–1073, 1993.
- [4] M. K. Ozkan, A. T. Erdem, M. I. Sezan, and A. M. Tekalp. "Efficient multiframe Wiener restoration of blurred and noisy images." *IEEE Trans. Image Processing*, 1(4):453–476, 1992.
- [5] S. P. Kim and Wen-Yu Su. "Recursive high-resolution reconstruction from blurred multiframe images." *IEEE Trans. Image Processing*, 2:534–539, 1993.
- [6] D. L. Snyder, T. J. Schulz, and J. A. O'Sullivan. "Deblurring subject to nonnegativity constraints." *IEEE Trans. Signal Processing*, 40(5):1143–1150, 1992.
- [7] R. L. Lagendijk, J. Biemond, and D. E. Boeke. "Identification and restoration of noisy blurred images using the expectation-maximization algorithm." *IEEE Trans. Acoust., Speech, Signal Processing*, 38:1180–1191, 1990.
- [8] J. W. Goodman. *Statistical Optics*. John Wiley & Sons, New York, 1985.
- [9] W. L. Root. "Ill-posedness and precision in object-field reconstruction problems." *J. Opt. Soc. Am. A*, 4(1):171–179, 1987.
- [10] D. L. Snyder, C. W. Helstrom, A. D. Lanterman, M. Faisal, and R. L. White. "Compensation for readout noise in CCD images." *J. Opt. Soc. Am. A*, 12(2):272–283, 1995.
- [11] D. L. Snyder and M. I. Miller. "The use of sieves to stabilize images produced with the EM algorithm for emission tomography." *IEEE Trans. Nucl. Sci.*, NS-32(5):3864–3871, 1985.
- [12] J. A. O'Sullivan. "Roughness penalties on finite domains." *IEEE Trans. Image Processing*, 4(9):1258–1268, September 1995.
- [13] C. A. Bouman and K. Sauer. "A generalized Gaussian image model for edge-preserving MAP estimation." *IEEE Trans. Image Processing*, 2:296–310, 1993.
- [14] J. A. Fessler and A. O. Hero. "Space-alternating generalized expectation-maximization algorithm." *IEEE Trans. Signal Processing*, 42(10):2664–2677, 1994.
- [15] J. A. Fessler and A. O. Hero. "Penalized maximum-likelihood image reconstruction using space-alternating generalized EM algorithms." *IEEE Trans. Image Processing*, 4(10):1417–1429, 1995.
- [16] C. A. Bouman and K. Sauer. "A unified approach to statistical tomography using coordinate descent optimization." *IEEE Trans. Image Processing*, 5:480–492, 1996.
- [17] H. T. Pai and A. C. Bovik. "Exact multichannel blind image restoration." *IEEE Signal Processing Letters*, 4:217–220, 1997.
- [18] G. Harikumar and Y. Bresler. "Perfect blind restoration of images blurred by multiple filters: Theory and efficient algorithms." *IEEE Trans. Image Processing*, 8(2):202–219, 1999.
- [19] T. J. Schulz, B. E. Stribling, and J. J. Miller. "Multiframe blind deconvolution with real data: Imagery of the Hubble Space Telescope." *Optics Express*, 1(11):355–362, 1997.
- [20] W. C. van Kampen and R. G. Paxman. "Multiframe blind deconvolution of infinite-extent objects." In *Proc. SPIE Vol. 3433, Propagation and Imaging through the Atmosphere II*, pages 296–307, 1998.
- [21] R. G. Paxman, J. H. Seldin, M. G. Löfdahl, G. B. Scharmer, and C. U. Keller. "Evaluation of phase-diversity techniques for solar-image restoration." *Astrophysical Journal*, 467:1087–1099, 1996.